A Zero-Gravity Instrument to Study Low Velocity Collisions of Fragile Particles at Low Temperatures

D. M. Salter,[1] D. Heißelmann,[2] G. Chaparro,[1,3] G. van der Wolk,[3] P. Reißaus,[4] A. G. Borst,[5] R. W. Dawson,[6] E. de Kuyper,[7] G. Drinkwater,[6] K. Gebauer,[2] M. Hutcheon,[6] H. Linnartz,[8] F. J. Molster,[1,9] B. Stoll,[2] P. C. van der Tuijn,[7] H. J. Fraser,[6] and J. Blum[2, *]

[1]*Leiden Observatory, Leiden University, Postbus 9513, 2300 RA, Leiden, Netherlands*
[2]*Institute for Geophysics and Extraterrestrial Physics,*
University of Braunschweig, Institute of Technology,
Mendelssohnstraße 3, 38106, Braunschweig, Germany
[3]*Kapteyn Astronomical Institute, University of Groningen, Postbus 800, 9700 AV, Groningen, Netherlands*
[4]*Space Technology & Applications Division, Kayser-Threde,*
GmbH, Wolfratshauser Straße 48, 81379, Munich, Germany
[5]*Dutch Space B.V., Postbus 32070, 2303 DB, Leiden, Netherlands*
[6]*Department of Physics SUPA (Scottish Universities Physics Alliance),*
University of Strathclyde, 107 Rottenrow East, Glasgow G4 0NG UK
[7]*Fijn Mechanische Dienst, Leiden Institute of Physics,*
Leiden University, Postbus 9513, 2300 RA, Leiden, Netherlands
[8]*Raymond and Beverly Sackler Laboratory for Astrophysics,*
Leiden Observatory, Postbus 9513, 2300 RA, Leiden, Netherlands
[9]*Netherlands Organization for Scientific Research, Council for the Physical Sciences,*
Postbus 93460, 2509 AL, The Hague, Netherlands
(Dated: June 22, 2009)

We discuss the design, operation, and performance of a vacuum setup constructed for use in zero (or reduced) gravity conditions to initiate collisions of fragile millimeter-sized particles at low velocity and temperature. Such particles are typically found in many astronomical settings and in regions of planet formation. The instrument has participated in four parabolic flight campaigns to date, operating for a total of 2.4 hours in reduced gravity conditions and successfully recording over 300 separate collisions of loosely packed dust aggregates and ice samples. The imparted particle velocities achieved range from $0.03\text{-}0.28\,\mathrm{m\,s^{-1}}$ and a high-speed, high-resolution camera captures the events at 107 frames per second from two viewing angles separated by either $48.8°$ or $60.0°$. The particles can be stored inside the experiment vacuum chamber at temperatures of $80\text{-}300\,\mathrm{K}$ for several uninterrupted hours using a built-in thermal accumulation system. The copper structure allows cooling down to cryogenic temperatures before commencement of the experiments. Throughout the parabolic flight campaigns, add-ons and modifications have been made, illustrating the instrument flexibility in the study of small particle collisions. *[Copyright Notice: The following article has been accepted by the* Journal of the Review of Scientific Instruments. *After it is published, it can be found at http://rsi.aip.org]*

I. INTRODUCTION

The origin of the Solar System and the formation of planets, including the enticing implications for the distribution of life in the universe, are key avenues pursued in modern astronomy by observational astronomers, theoretical physicists, and to a substantially smaller extent, experimentalists. Given the unresolvable scale size at interstellar distances, the embedded environment, and the uncertainty of the dominating physical processes, it is a challenging task to understand planetary origins when applying observation techniques and theoretical modeling alone. Now recent progress in laboratory experi-

ments has yielded insight into particle collisions during the *initial* planet formation stages (e.g. growth to mm-sizes), complementing observational and theoretical work while providing a repeatable and consistent recipe to describe individual particle interactions [1]. In this paper, we present a new laboratory instrument to test the *next* stage (e.g. growth to cm-sizes) of coagulation theory, which is the leading scenario for planet formation that describes a collisional growth mechanism.

The scientific goals specifically target the properties of fragile, mm-sized ice and dust aggregates during collisions. The aggregates are analogous to the prevalent material found in proto-planetary disks around young stars and therefore are believed to be the progenitors for rocky Earth-like planets, as well as the core beginnings of gas giants like Jupiter [2, 3]. But until now the physical processes governing this crucial *intermediate* stage of collisional growth (from mm- to km-sizes) have remained

---
*Author to whom correspondance should be addressed; electronic mail: j.blum@tu-bs.de

largely uninvestigated. The most challenging aspects to these studies involve re-creating the reduced-gravity environment for the timescales necessary to observe particle growth through collisional sticking mechanisms. In this respect, ground-based drop tower experiments [4, 5], parabolic flight maneuvres [6], space shuttle payload missions [7, 8], and the space-based laboratory on board the International Space Station (ISS) [9] offer unique ways to counter the effects of the Earth's gravitational field by creating a temporary condition of weightlessness.

The indirect detection of more than 300 extra-solar planets suggests that planet formation might well be a commonly occuring process, even a fundamental by-product of star formation. In previous laboratory and microgravity experiments, the inital growth period for silicate dust particles (up to mm-sizes) has already been shown to occur quickly and effectively, due to van der Waals forces, achieving a sticking probability of unity during particle collisions of low relative velocities ($v_c \leq 1 \, \mathrm{m \, s^{-1}}$) that result in larger, fluffy and porous, aggregate structures [1]. Observationally, spectroscopic studies of silicate dust emission features at 10 and 20 μm emanating from a large sample of circumstellar disks around young forming stars that exhibit convincing evidence of the initial grain growth process from small, sub-micron interstellar particles up to aggregates of several microns [10, 11]. In addition, probing these disks at longer, millimeter wavelengths reveals a slower drop-off in emission than expected for some sources, which can be explained by a population of particles that have already grown to millimeter sizes [3, 12].

The conclusions of both observation and experiment are consistent with coagulation theory in these earliest stages, but the dominant physical processes begin to change in unidentified ways as particles grow larger and begin to settle within the circumstellar disk midplane. We know that once the objects reach km-sizes, they possess sufficient gravitational attraction to capture and retain additional mass, kicking off a gravitationally-dominated period of runaway growth leading to planetary status [13, 14]. But how do mm-sized aggregates attain km-sizes, and thereafter runaway growth? What are the dominant processes or conditions that allow, or prevent, particles from growing beyond cm-sizes for which observational diagnostics are lacking? It is this *intermediate* growth stage that may be the crux to questions regarding the ease, efficiency, and proliferation of planets and planetary systems in the universe. It is also here where our physical interpretation is insufficient, and thus where we shall focus our current experimental efforts and draw comparisons to recent theoretical models.

At the intermediate growth stage, the particle size and the density of particles required to guarantee a chance collision within a 4-10 second drop tower experiment, is prohibitive to a video analysis capable of capturing an unobstructed view. Instead, a more direct design was developed to initiate and observe individual collisions. For this, parabolic flight was selected to preserve the flexibility and diversity of the experiments in 22-second intervals. Parabolic flights take place on board a specially designed Airbus A300 aircraft and are organized regularly by the European Space Agency (ESA) and the German Space Agency (DLR), and they are operated by the French company, Novespace. During each flight campaign, approximately 10-15 experiments are accomodated on 3 separate flights of 30 parabolic trajectories each. Between parabolas, regular ($1g$) horizontal flight is maintained for several minutes to give experimenters working alongside their setups a chance to quickly review the data collected and to make necessary adjustments or corrections to their setup. In total, one flight campaign offers a combined weightless (or microgravity) period of approximately 30 minutes.

To account for the low gas densities of circumstellar disks, our instrument uses laboratory pumps and a vacuum chamber. Previous experimental studies give us an idea of the aggregate structure of the mm-sized particles expected in the solar nebula from collisional sticking [15, 16]. Observations of young disks tell us about the environment and composition, including the temperature range (30-1500 K) and the presence of ices, respectively. Our design is able to achieve cold temperatures ($\simeq 250$-$300 \, \mathrm{K}$) to probe dust interactions, as well as cryogenic temperatures ($\simeq 80$-$250 \, \mathrm{K}$) where ices may play an important role in offering additional routes to more efficient sticking processes. In addition, theoretical work reveals the kinematics in the layers of the disk at these temperatures [2]. For the particle sizes that we wish to study, the aggregates are just beginning to de-couple from the pressure-supported gas that has governed their motion up to this point and kept them suspended higher in the disk atmosphere. This growth causes them to sink toward the dense midplane of the disk, giving the larger particles a non-zero relative velocity with respect to the other (smaller) particles still coupled to the turbulent gas. This defines the collision velocities expected, on the order of $0.10 \, \mathrm{m \, s^{-1}}$, for the planet-forming regions we are studying [2, 17]. These velocities do, however, present a great challenge to ground-based studies where the Earth's gravitational field makes relative particle velocities of $\ll 1 \, \mathrm{m \, s^{-1}}$ very hard to achieve, and where it may prevent, or favor, sticking processes unrealistically.

In October 2006, we proved our experimental setup during ESA's 45th Parabolic Flight Campaign on the Novespace premises at the Bordeaux-Merignac airport in Bordeaux, France. Additional flight campaigns followed, including the November 2007 (ESA and DLR) campaigns and the April 2008 DLR campaign, all also held in Bordeaux. This paper reports on the instrument design. In Section II we describe the separate components of the experiment, in Section III we report on the instrument performance in microgravity, and in Section IV we offer a short summary of some preliminary results for the purpose of illustrating the effectiveness of the instrument with respect to our scientific goals.

II.   EXPERIMENT DESIGN OVERVIEW

The science goals driving our experiment design are the collisional properties of fragile, mm-sized, proto-planetary dust and ice analogs in young circumstellar disks. To obtain a large statistical sample of this collision behavior in a simulated early proto-planetary disk environment, a particle storage and cooling system built from copper (Sect. II A) was developed to fit inside a cylindrical vacuum chamber (of diameter 250 mm and height 290 mm), and to operate over a broad range of cold (250-300 K, for proto-planetary *dust* analogs) and cryogenic temperatures (80-250 K, for proto-planetary *ice* analogs). A hydraulically-driven, synchronized particle acceleration system rapidly initiated collisions during the initial flight, but was later replaced by two synchronized electrical DC-motors operating in a master-and-slave configuration (Sect. II C). For the purpose of the experiments, the functionality of these setups are identical in every way, differing only in the synchronization design. Both acceleration systems specify the velocity and trajectory of two separate dust or ice analogs approaching from opposite directions so that the projectiles either collide simultaneously with a removable, dual-sided, centrally-located dust/ice target (Sect. II D) – or with one another – within the field of view of a high-speed, high-resolution imaging and data recording system (Sect. II E). Finally, the vacuum chamber and the support equipment were fit into two separate aluminum-strut support racks to be placed on board the parabolic flight aircraft, according to safety guidelines. A blueprint of the overall experiment design is shown in Fig. 1 and the following sections describe the separate components and capabilities in greater detail.

A.   Particle Storage and Cooling

An original design for particle storage was engineered based on the requirements that the setup is capable of operating at low and cryogenic temperatures, possesses fast and controlled collision reloadability, obeys physical size restrictions, has maximum sample capacity, and is in accordance with safety regulations for parabolic flights. The result is a cylindrical storage device, or particle reservoir, built from copper (see Fig. 2). It has a diameter of 180 mm and stands 110 mm high. In the upper half of the reservoir we drilled 180 identical, cylindrical compartments (each of diameter 8 mm and depth 9 mm) situated at regular intervals (separated by a turn of 12.5°) in a double-helix pattern, such that each hole is aligned exactly opposite a corresponding hole. When fully loaded in this configuration, 90 separate collisions between fragile particles (or 180 collisions of particles and central target) can be performed. During the 2007 and 2008 follow-up flights, an additional storage chamber of the same dimensions was conceived to hold 64 compartments of slightly
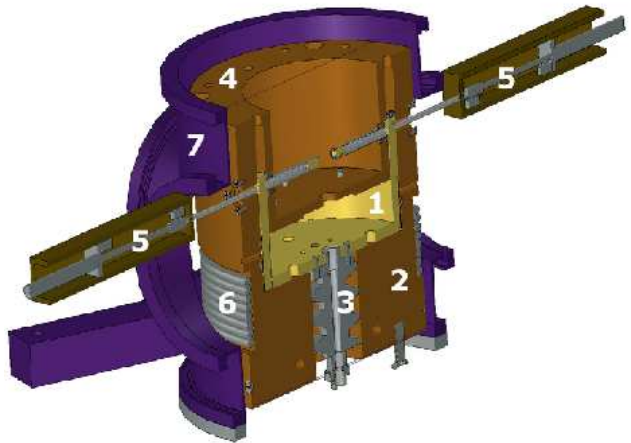

FIG. 1: (Color online) A CAD schematic showing a cut through the center of the experiment chamber. The particle storage device (1) sits on top of the thermal reservoir (2) built of copper. The particle storage unit rises up and down with a cork-screw system (3) to rotate additional particles into the fixed line of fire. A copper shield (4) protects the storage device from thermal irradiation. The two "firing" pistons of the particle acceleration system stretch from opposite sides beginning outside the side flanges and continuing toward the center of the chamber (5). The whole system is chilled through contact with a copper tubing (6) that contains a flow of liquid N_2. The entire instrument is situated within a vacuum chamber (7). Collisions are monitored from above with the image acquisition system via a transparent viewport on the top flange.

larger volume (for 32 collision pairs). The 64 holes have a diameter of 16 mm with a 24° turning separation. Built this time of aluminum, the new particle storage device can be easily swapped for the original to probe the collision properties of larger particles, up to 15 mm.

On the lower half of the copper reservoir exterior, below the storage compartments, vertical grooves were cut into the copper (see Fig. 2). This way a small gear (e.g. 20 mm in diameter and 10 mm high), situated to the side of the storage unit, and possessing the same groove pattern as the storage unit, can be used to turn the selected reservoir unit (automatically or manually) with a hand wheel that passes out of the chamber through the bottom flange. Later, due to difficulties operating the small gear at cryogenic temperatures (80-250 K), the rotation of the sample repository was revised, such that the handwheel now directly couples to the brass-made cork-screw system (see Fig. 1, label 3) with a double-Cardanic joint to prevent canting. For this reason, a similar groove pattern was no longer necessary on the bottom half of the aluminum version of the storage unit.

Since cryogenic liquids and pressurized vessels are prohibited during flight, it was necessary to devise a thermal accumulation system to achieve, and maintain, cold and cryogenic temperatures for several uninterrupted hours. A copper construction was deemed most suitable based

on copper's high heat capacity per unit volume, high thermal conductivity, and ease of manufacturing for adjustments and customization. Thus, the copper *particle* reservoir is situated on top of a 45 kg copper *thermal* reservoir, or copper block (see label 4 in Fig. 3). The two reservoirs (particle and thermal) fit together via a custom-made, quintuple thread (essentially a large screw of diameter 30 mm and length 70 mm), which is firmly attached to the bottom of the particle reservoir and fits a hollowed out groove in the thermal block. The thread steadies the particle reservoir as it raises out of, or lowers into, the thermal block during rotation (supporting a height change of 5 cm). This vertical movement allows us to increase the storage capacity, by achieving a continuous, winding row of samples that completes two rotations of the reservoir. In this setup, more samples can be loaded in front of the fixed firing system during flight, all the while maintaining thermal contact between the storage device and the thermal reservoir for the duration of the experiment.

Finally, a 10 mm thin, U-shaped copper casing, or cover (label 2 in Fig. 3), slips over the particle reservoir on top. This cover shields the storage device from external radiative warming effects, and serves to "seal" the fragile samples in their respective compartments, until primed for release. The cover is fixed to the thermal block during flight, locking the (loaded) reservoir inside and fixing the alignment. In combination with the quintuple support thread, the slip cover helps prevent the sample repository from tilting while still leaving enough vertical space within (above and below) so that the reservoir can wind up and down freely. Together the entire copper construction, shown in Fig. 3, is then placed within the vacuum chamber atop insulation "feet" constructed from Polyetheretherketones (PEEK).

B. Cryogenic Operation

Once sealed, the vacuum chamber is pumped using the combination of a turbo-molecular pump (TMP) and a membrane pump in series. When a pressure of $< 10^{-2}$ mbar is achieved, cooling of the internal environment can commence without any significant heat transfer due to the residual gas inside the chamber. This prevents the vacuum chamber from sweating or getting frosted on the outside. The best vacuum attainable in this setup is 10^{-6} mbar. Liquid N_2 (LN2) enters the chamber through a LN2 feedthrough on the bottom flange. It is connected on the inside to flexible copper tubing that has been molded around the thermal reservoir (label 3 in Fig. 3). The fluid winds upwards, conductively cooling the copper tubing, the copper block, and finally the particle reservoir and radiation shield. K-type thermocouples monitor the system temperature at up to 8 separate (and distributed) locations during this process. The residual nitrogen gas and liquid that reaches the top of the coiled tube flows
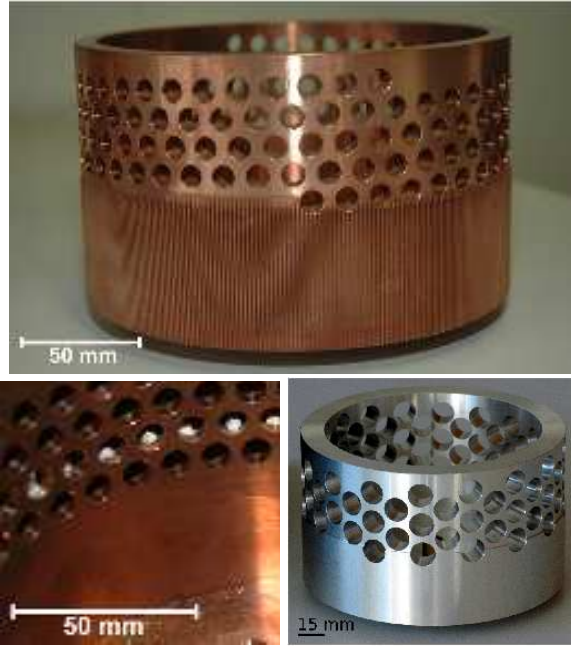

FIG. 2: (Color online) At top, the original copper particle storage device with the storage compartments on the upper half and the vertical grooves to fit a gear on the lower half. Below left, individual compartments in one row are filled with the fragile mm-sized dust aggregates described in the text (see Sect. III). At right, the aluminum version with 64 holes for larger particle collisions. The grooves are no longer necessary with the revised handwheel system (see Sect. II A).

FIG. 3: (Color online) The copper construction affixed atop the bottom flange of the vacuum chamber and isolated from the external environment by insulating "feet" constructed from PEEK. Label 1 shows a glimpse of the reservoir via the entrance portal for the firing system (see Sect. II C); label 2 identifies the radiation shield; label 3 indicates the copper tubing for the LN2; and label 4 highlights the thermal block.

FIG. 4: A close-up view of one of the two pistons in the new design. The labels indicate the DC-motor (1), the gear box (2), the stainless steel lead screw (3) with both the front and back switches, and finally, the vacuum feedthrough (4) with a protective cover.

back out of the chamber through the second "exit" port. At no point does LN2 flow freely within the chamber itself.

Cryogenic temperatures of ~ 80 K can be achieved with our setup using approximately 45 liters of LN2, when pumped through the flexible copper tubing for 90 minutes. Once the flow of LN2 is stopped, the system heats up at a rate of approximately $5 \, \mathrm{K \, h^{-1}}$ if left unto itself under our best vacuum (see Sect. III for data taken during an experiment). After a completed series of experiments, but before the vacuum seal is broken, the entire system can be brought back up to 300 K by a heat rope wound around the copper base block, which is triggered via an external electrical control unit. The heat rope, which is 34 m long, has a cross-section of 3 mm and a heat output of 840 Watts.

C. Particle Acceleration System

To study astrophysically important collisions in this setup, we require: very low impact velocities, constant acceleration with no spiking due to the delicate nature of the aggregates, clean release of the particles, and precise alignment and synchronization of the trajectories to intersect within the camera's field of view. Although our fluffy and porous dust aggregates are capable of sustaining accelerations up to $100 \, \mathrm{m \, s^{-2}}$, we limit the maximum acceleration of the particles to $10 \, \mathrm{m \, s^{-2}}$ in order to prevent compaction, and thus preserve their astrophysical aggregate design.

In the updated design, a versatile piston driving mechanism was implemented using a master-and-slave DC-motor-system combination to replace a hydraulically-driven setup. Two synchronized pistons approach the center of the particle reservoir (and chamber) from fixed positions opposite one another. The piston back-ends extend about 0.5 m outside the vacuum chamber and each piston rod must pass through two separate vacuum feedthroughs before finally breaching the internal environment. Thus, the additional pass-through introduces an intermediate vacuum environment by applying

a chamber extension piece. This design reduces the leak rate associated with the moving parts, as the extensions can also be pumped in parallel, if necessary, although pumping proved nonessential in our construction. Inside the chamber, the stainless-steel piston rods first pass through the outer radiation shield and then through one of the storage compartments, collecting a dust or ice aggregate on each side with each concave-shaped piston head. The pistons accelerate the samples towards the center of the chamber, and one another, guided along two 80 mm long trajectory-confining tubes, before stopping abruptly (for particle detachment in cases of sticking) once the samples have achieved the intended velocity.

D. Removable Target Holder

To simulate impacts of our mm-sized particles against much larger proto-planetary dust aggregates, a removable target holder was crafted from copper to fit within the collision space between the two guiding tubes (see Fig. 5). The target is 17 mm in diameter and approximately 2 mm deep. The dual-sided, concave structure allows us to affix loose or compacted dust or ice samples into the mold on each side and attach the samples with vacuum grease. The embedded target sample is representative of a larger, possibly more rigid, compact, and sturdier proto-planetary aggregate or particle. The target holder itself is attached at its base to the particle storage device. This allows it to turn throughout the experiment (synchronized with the particle storage unit) and offers a wide range of impact angles to be studied, from $0°$ (head-on) to approximately $75°$ (almost glancing, but before the target is edge-on and begins to block the exits of the guiding tubes). The largest impact angles therefore place additional limitations on the total number of collisions that can be executed when the target is in place. To remove this constraint at any time during the experiment, a solenoid release mechanism allows the

FIG. 5: (Color online) The dust-filled target (1) is the square piece at the center of the collision space. To the left and right are the two guiding tubes (2) within which the dust aggregates are accelerated. Above center, the solenoid release mechanism (3) for the target is visible (See Sect. II D).
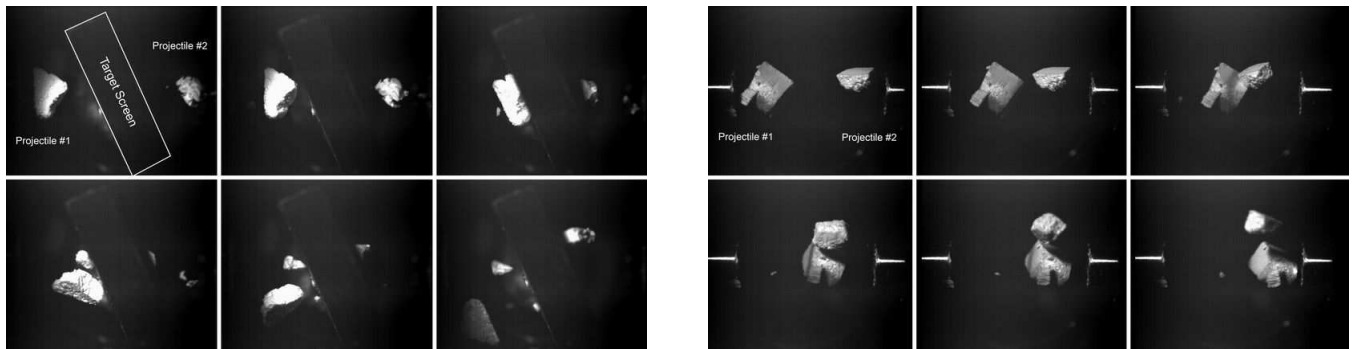
FIG. 6: (Color online) Image sequences recorded during ESA's 45$^{\text{th}}$ Parabolic Flight Campaign. The sequence at left are frames showing aggregate-target dust collisions at a particle velocity of $0.2\,\text{m}\,\text{s}^{-1}$ and ambient temperature. The time-series on the right shows an aggregate-aggregate collision at a relative velocity of $0.4\,\text{m}\,\text{s}^{-1}$. All frames measure approximately 24 mm across and capture the end of the guiding tubes, which are more clearly visible in the right-hand sequence. In both cases, the dust aggregates do not stick, but instead rebound after the collision.

target holder to drop out of the way of the collision path during normal ($1g$) horizontal flight. Using a 24V DC signal, a lifting magnet is triggered to pull on a small bolt that releases the two latches that fix the target in place. Once released, and the target has dropped out of the collision space, an additional latch fixes the target in this lowered position until the vacuum chamber can be safely re-opened and the target reset manually. Then, from this point forward, only particle-particle collisions are possible.

E.   Data Acquisition and Imaging

Capturing the collision events is achieved by a high-speed, high-resolution state-of-the-art CMOS camera and a recorder computer system that is capable of writing a sustained maximum data rate of $133\,\text{MB}\,\text{s}^{-1}$ directly to the hard disks for an uninterrupted duration of about 33 minutes. The latter feature makes the system indispensable for parabolic flight experiments with only short breaks between the experiments, which do not provide sufficient time for a read-out of imaging systems with internal memories (either camera internal or frame grabber on-board memories).

The camera is operated at 107 frames per second (fps) and features $1280\,(\text{h}) \times 1024\,(\text{v})$ pixels with 8 bit pixel depth (gray scale), a pixel size of $12\,\mu\text{m} \times 12\,\mu\text{m}$, a fill factor of 40%, and a Base/Full CameraLink$^{\circledR}$ interface. The digital recording system is a high-performance PC system that, in this special configuration, is able to handle and store the generated data streams of the camera. Its most prominent features comprise 2 CPUs with $2.66\,\text{GHz}$ each, a PCI-X based frame grabber with $2\,\text{GB}$ of internal memory, and 4 SATA-I hard disks totaling $260\,\text{GB}$ when bundled as a RAID 0 array.

The camera is mounted on top of the chamber and captures the collisions below through a transparent viewing port. Two synchronized stroboscopic Xenon flash lamps of $1\,\mu\text{s}$ flash duration are mounted on the top flange and provide for shadow-free illumination of the collision volume. The flash lamps are synchronized with the camera via a small strobe pulse adaptor box, which reverses and amplifies the control pulses that are generated by the camera towards the illumination source. To retrieve imaging information from multiple viewing angles with only one camera, a 3D optics system was recently introduced, which uses a beam splitter placed above the collision space to capture light from two vantage points separated by either $48.8°$ or $60.0°$. The field of view covers a horizontal grid area of approximately $24\,\text{mm} \times 20\,\text{mm}$ at the focal distance. The focal depth limits the (focused) vertical range to $5\,\text{mm}$ near the collision plane. This places limitations on ground-based testing of the setup when used for the lowest available velocity settings.

III.   PERFORMANCE IN MICROGRAVITY

The system performance in microgravity proved stable, reliable, and accurate when flown at ambient ($300\,\text{K}$) and cryogenic ($130\text{-}180\,\text{K}$) temperatures in vacuum. Here we will focus our performance analysis entirely on the inaugural flight (October 2006), which was flown at ambient temperatures. Our fragile samples were selected to simulate dust grains in the relatively warm parts ($300\,\text{K}$) of the proto-planetary disk. These dust aggregates were assembled from $1.5\,\mu\text{m}$ monodispersed monomer SiO_2 spheres using Random Ballistic Deposition [18], measured 0.2-6 mm in diameter, and were 85% porous [15] giving an approximate mass range of 0.01-3.0 g. They possessed translational velocities of $0.10\text{-}0.28\,\text{m}\,\text{s}^{-1}$ (the upper range of the available experiment velocities) as they entered the collision space, accelerated by the original hydraulically-driven piston setup. This imparted velocity range tested during the inaugural flight was slightly lower than expected from ground tests, but consistent overall. Synchronization of the particle acceleration sys-
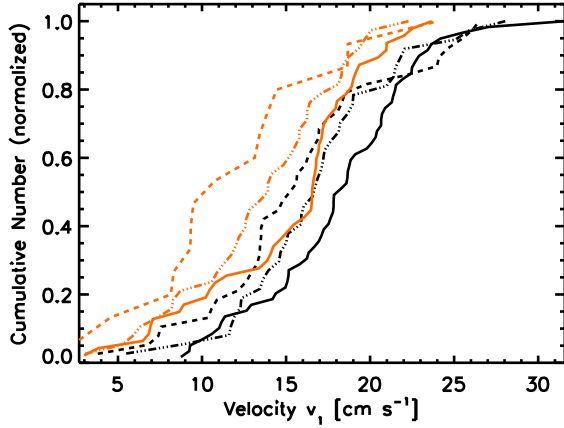
FIG. 7: (Color online) The cumulative number (normalized) of all particles in the inaugural flight with an exit velocity $\leq v_1$, using the hydraulically-driven piston setup. The solid, dotted, and dashed lines represent three velocity settings A, B, and C (intended to serve particles at speeds of 0.17, 0.19, and $0.20\,\mathrm{m\,s^{-1}}$). Black and orange lines differentiate between the right and left piston. Each line is normalized by the total number of observed particles per piston at that velocity setting. For the right piston, this is 59, 37, and 38 for setting A, B, and C, respectively. For the left piston, this is 47, 38, and 15 for each velocity setting. The plot illustrates how switching to a lower velocity setting indeed results in lower velocities, and that the left-hand piston consistently delivers particles at a slightly higher speed.
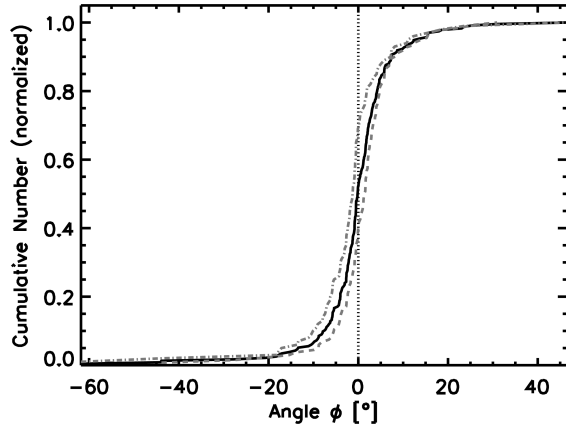
FIG. 8: (Color online) The cumulative number (normalized) of all projectiles in the inaugural flight delivered within an exit angle $\leq \Phi$. The solid line represents all particles whereas the dashed and dash-dotted curve represent the particles from the left and right piston, respectively. The distribution is very steep, showing that the angular distribution is very narrow.

tem proved flawless and all collisions were easily observed to occur at the center of the collision volume, and within the camera's focal plane.

We began this first experiment with aggregate and target collisions of dust. Once we were satisfied with the resulting number of central target collisions,

we dropped the target and proceeded to study dust aggregate-aggregate collisions. Both scenarios in this initial experiment offer important astrophysical insight into grain growth by probing two *collisional* velocity ranges (0.10-$0.28\,\mathrm{m\,s^{-1}}$ for aggregate-target collisions and 0.20-$0.56\,\mathrm{m\,s^{-1}}$, or twice the *imparted* velocities, for aggregate-aggregate collisions), as well as the influence of relative sizes (e.g. small projectile against a large target versus similarly-sized colliding aggregates). Examples of the data for both types of collision events are given in recorded image sequences in Fig. 6. In addition, the histograms in Fig. 7 and 8 show the distribution of the exit angles and velocities for all particles with this setup, illustrating the accuracy and consistency of particle speeds and trajectories, as designed.

We achieved 3-4 collisions per 22-second microgravity period with manual rotation of the particle reservoir and visual verification of the alignment. This was one collision more per parabola than initially anticipated when designing and testing an automated system for exit velocities of 0.10-$0.28\,\mathrm{m\,s^{-1}}$ (e.g. during our first and only flight in 2006). Of course, for slower exit velocities (0.03-$0.15\,\mathrm{m\,s^{-1}}$) when using larger particles in the aluminum storage unit during the follow-up campaigns, the number of possible collisions per parabola is reduced to 1-2. Ultimately, the manual rotation system proved far more reliable and flexible than the autonomous design. This was largely a result of a hand-operated turning system, which could rotate the coliseum with larger accelerations and abrupt stops during alignment.

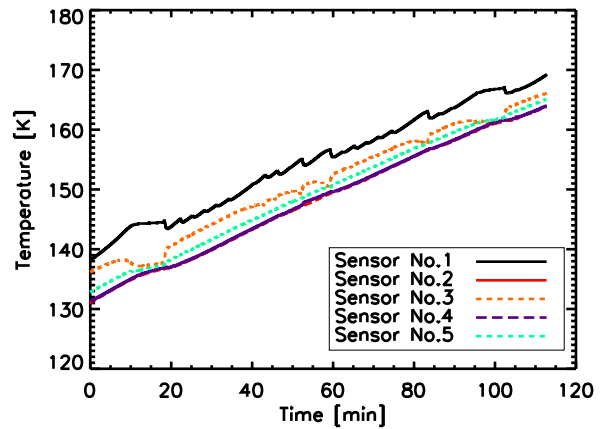Finally, the additional cryogenic functionality, as

FIG. 9: (Color online) The plot above shows how the temperature evolves during a typical parabolic flight at cryogenic temperatures and low ($10^{-2}\,\mathrm{mbar}$) vacuum. Small fluctuations ($\pm 4\,\mathrm{K}$) result from different contact between the thermocouple and the instrument during the 0, 1, and $2g$ phases of the flight. Thus thermocouples located on top (#3) or below (#1) the structure will report mirrored fluctuations, while smaller effects are seen for thermocouples attached to the side.

stated, also allows for the experimentation with interstellar ice analogs, since the abundance of ice in proto-planetary disks is high, as supported by the high abundance of icy bodies in the outer solar system, including the Kuiper-belt objects, icy moons, and comets. In the 2007 and 2008 follow-up flights, we initiated more than 64 additional collisions of (larger) dust aggregates at cold temperatures (250 K) and slower velocities, whereby 26 clean collisions could be analyzed, and the rest were contaminated either by third-party collisions with previously-fired particles remaining in the collision area, or by other complications. Finally, the experiments at cryogenic temperatures (130-180 K) produced more than 113 collisions of ice particles to be analyzed.

The temperature gradients during ground-based and in-flight testing measured just a few Kelvin across the entire copper structure, even throughout pre-flight cooling of the experiment from 300 K down to 80 K via the LN2 system described in Sect. II B. However, due to the weak pumping capabilities available during flight, the system operated more often under a pressure of 10^{-2} mbar. This translated to a larger warm-up rate during the cold ice experiments, as shown in Fig. 9 where the warming rate for a two-hour flight was measured to be $\sim 15\,\mathrm{K\,h^{-1}}$. We note that the change in the initial cooling temperature of 80 K to the 130 K that was measured at the start of the experiment (Fig. 9), is due to the time between closing of the aircraft doors and the time to reach the approved air space to perform the flight maneuvre.

IV. CONCLUSIONS

Our instrument design to probe the collisions of fragile particles at low velocities certainly proved successful in its inaugural run at ambient temperatures (300 K) in vacuum, as well as during the follow-up campaigns at cold (250 K) and cryogenic (130-180 K) temperatures. For the ambient dust experiments in the 2006 campaign, the 6 mm in diameter and 85% porous SiO_2 aggregates possessed translational velocities from 0.10-0.28 m s^{-1}, resulting in particle-particle collisional energies of 1-5 μJ and particle-target collisional energies of 0.5-2.5 μJ. The majority of all collisions (roughly 80-90%) resulted in semi-elastic rebounding events, likely due to aggregate compaction. Fragmentation occurred in about 10% of the aggregate-aggregate collisions, but played a much smaller role during particle-target impact events. And finally, sticking was observed only in 10% of the particle-target collisions. However, the forces responsible remain unclear and warrant additional investigation. Still, the sticking and fragmentation statistics from this inaugural campaign suggest that we are probing a critical transition region for the collision velocities of dust agglomerates. And eventually it is the competition between sticking probability, fragmentation efficiency, mass exchange, and compaction behavior during encounters that helps shape disk lifetimes and the effectiveness of planet formation via grain coagulation. These early results from dust collisions at ambient temperatures exhibit the flexibility and power of this instrument in the study of particle collisions. Planned refinements to the experiments that have not yet been implemented include: icy additives of amorphous (in place of hexagonal) crystallographic structure, and the use of cryogenic temperatures (< 130 K) and high vacuum.

[1] J. Blum and G. Wurm, ARA&A **46**, 21 (2008).

[2] S. J. Weidenschilling and J. N. Cuzzi, in *Protostars and Planets III*, edited by E. H. Levy and J. I. Lunine (1993), pp. 1031–1060.

[3] A. Natta, L. Testi, N. Calvet, T. Henning, R. Waters, and D. Wilner, in *Protostars and Planets V*, edited by B. Reipurth, D. Jewitt, and K. Keil (2007), pp. 767–781.

[4] J. Blum, G. Wurm, T. Poppe, S. Kempf, and T. Kozasa, Advances in Space Research **29**, 497 (2002).

[5] D. Langkowski, J. Teiser, and J. Blum, Astrophys. J. **675**, 764 (2008).

[6] J. E. Colwell, S. Sture, M. Cintala, D. Durda, A. Hendrix, T. Goudie, D. Curtis, D. J. Ashcom, M. Kanter, T. Keohane, A. Lemos, M. Lupton, and M. Route, Icarus **195**,

908 (2008).

[7] J. Colwell and M. Taylor, Icarus **138**, 241 (1999).

[8] J. E. Colwell, Icarus **164**, 188 (2003).

[9] S. G. Love and D. R. Pettit, in *Lunar and Planetary Institute Conference Abstracts*, edited by S. Mackwell and E. Stansbery (2004), vol. 35 of *Lunar and Planetary Institute Conference Abstracts*, p. 1119.

[10] J. Kessler-Silacci, J.-C. Augereau, C. P. Dullemond, V. Geers, F. Lahuis, N. J. Evans, II, E. F. van Dishoeck, G. A. Blake, A. C. A. Boogert, J. Brown, J. K. Jørgensen, C. Knez, and K. M. Pontoppidan, ApJ **639**, 275 (2006).

[11] E. Furlan, L. Hartmann, N. Calvet, P. D'Alessio, R. Franco-Hernández, W. J. Forrest, D. M. Watson, K. I. Uchida, B. Sargent, J. D. Green, L. D. Keller, and T. L. Herter, ApJS **165**, 568 (2006).

[12] D. Lommen, C. M. Wright, S. T. Maddison, J. K. Jørgensen, T. L. Bourke, E. F. van Dishoeck, A. Hughes, D. J. Wilner, M. Burton, and H. J. van Langevelde, A&A **462**, 211 (2007).

[13] G. W. Wetherill and G. R. Stewart, Icarus **77**, 330 (1989).

[14] G. W. Wetherill and G. R. Stewart, Icarus **106**, 190 (1993).

[15] J. Blum, R. Schräpler, B. J. R. Davidsson, and J. M. Trigo-Rodríguez, ApJ **652**, 1768 (2006).

[16] J. Blum, in *Astrophysics of Dust*, edited by A. N. Witt, G. C. Clayton, and B. T. Draine (2004), vol. 309 of *Astronomical Society of the Pacific Conference Series*, p. 369.

[17] S. J. Weidenschilling, Icarus **127**, 290 (1997).

[18] J. Blum and R. Schräpler, Physical Review Letters **93** (2004).